Acta Mech
https://doi.org/10.1007/s00707-026-04782-7

ORIGINAL PAPER

Snježana Milovanović · Josef Kiendl · Yury Vetyukov

Isogeometric approximation of shear strain for rod contact problems

Received: 20 January 2026 / Revised: 28 May 2026 / Accepted: 2 June 2026
© The Author(s) 2026

Abstract A novel framework for modelling shear-deformable rods undergoing large deformations, with a focus on contact problems, is introduced in this paper. By treating the shear strain as an independent variable rather than the rotation angle customary in Timoshenko-type formulations we benefit from a two-stage solution strategy. A computationally efficient Bernoulli–Euler solution is first obtained and subsequently used as a reference state, from which the release of the unshearability constraint leads to rapid convergence toward a neighbouring shear-deformable configuration. Exploiting the smallness of the resulting deformation change further enables an incremental formulation of the rod theory that delivers accurate results at minimal additional cost. In weakly nonlinear settings, a single linear correction step proves sufficient, whereas problems involving contact require a Newton-type iterative scheme. The proposed framework is implemented using an isogeometric discretization with freely adjustable continuity of the approximation. Numerical examples with available analytical solutions demonstrate improved efficiency compared to the classical Timoshenko formulation, fast convergence with respect to mesh refinement, and reliable resolution of pronounced contact pressure peaks. The final example of a belt-pulley contact problem shows the potential of the proposed approach in a practically relevant setting.

1 Introduction

Shear compliance needs to be taken into account when modelling relatively thick beams and rods, whose size of the cross-section becomes comparable to their length. Being associated with the names of Timoshenko, Reissner and Cosserat, respective theories were derived and investigated in the literature in many ways. A significant contribution to the field was done by H. Irschik, who derived Reissner's large-displacement finite-strain beam theory based on continuum mechanics in [1,2] along with J. Gerstmayr. Further theoretical investigations concerning shear deformable rods were presented by H. Irschik in [3,4]. For the direct approach to rods as material lines from the standpoint of the principle of virtual work we refer to [5,6] as well as to the broadly known treatises [7,8].

S. Milovanović
Department of Mechanics and Theory of Structures, Faculty of Architecture, Civil Engineering and Geodesy, University of Banja Luka, Bulevar vojvode Petra Bojovića 1A, 78000 Banja Luka, Bosnia and Herzegovina

J. Kiendl
Institute for Engineering Mechanics and Structural Analysis, University of the Bundeswehr Munich, Werner-Heisenberg-Weg 39, 85577 Neubiberg, Germany

Y. Vetyukov (✉)
Institute of Mechanics and Mechatronics, TU Wien, Getreidemarkt 9, 1060 Vienna, Austria
E-mail: yury.vetyukov@tuwien.ac.at

Published online: 29 June 2026

A voluminous body of literature is devoted to the numerical treatment of contact problems featuring elastic rods, see e.g. [9,10]; for the problem of a beam-to-beam contact we refer to [11]; a refined continuum mechanics investigation is given in [12]. Since the works [13] and [14] it is known, however, that the shear deformability – and possibly other modes of deformation related to the thickness compression—becomes crucial for the local distribution of the contact pressure near the boundaries of the contact zone. Shear compliance regularizes the solution, which thus becomes more approachable for numerical analysis because of the absence of concentrated contact interactions [15]. Moreover, from the physical point of view, it strongly determines the local stick–slip behavior for moving belt-pulley problems with friction [16–18]. For the analytical solutions of the static belt-pulley contact problem, which we use later for validating the simulation results, we refer to [19–22].

In the present contribution we pursue the idea of an independent parameterization of the shear strain field in addition to the configuration of the centerline of the rod. The same idea has been presented for shells and plates in [23–25], where it was shown that the resulting formulations are free of shear locking by construction. This kind of approach resides between the common displacement and rotation driven parametrization of the deformed state and the advanced technique of using the strain fields as primary variables and reconstructing the deformed shape by integration, which has certain advantages e.g. in modelling flexible manipulators in robotics [26]. Allowing to enable and disable shear at will by merely including the respective degrees of freedom into the energy minimization problem or excluding them, the present approach has a potential of being computationally superior in comparison to the standard Timoshenko model also in the contact problems. Two variants of the shear parametrization are presented analytically and demonstrated in application to several benchmark problems in the following. While showing good correspondence to standard numerical and analytical solutions using Timoshenko theory, the novel models are demonstrated to require less CPU time for obtaining converged results. The reason is the smallness of the increment on top of the computationally cheaper solution for the shear rigid Bernoulli-Euler model.

The numerical investigations below feature an isogeometric (IGA) approximation of independent variables such as centerline geometry, rotation of the cross-sections or shear strains. Besides the known treatises on IGA [27,28] we mention applications to plane bending of beams [29], vibration analysis [30,31] and shell analysis [32,33]. Among the variety of contributions on IGA for contact problems we mention [34] with the focus on the geometric basis and smoothness; a comparison to standard finite element analysis is presented in [35]; for mortar-based contact formulations see [36]; T-splines are discussed in [37]; for an IGA collocation method for contact of Cosserat rods we refer to [38]; the effect of varying-order NURBS discretization is studied in [39]. In the context of the present investigation, IGA enables studying the interplay of the degree of continuity of approximation on the convergence behavior and accuracy of the solutions of contact problems with independent shear parametrization.

2 Models based on classical rod theories

We consider an extensible, shear-deformable planar rod, with its deformed configuration illustrated in Fig. 1. The rod axis (centerline) is parametrized by the material coordinate $s \in [0, L]$, with the position vector defined by the relation:

$$\boldsymbol{r}(s) = x(s)\,\boldsymbol{i} + y(s)\,\boldsymbol{j}. \tag{1}$$

Here, $x(s)$ and $y(s)$ denote the coordinates of a material particle in the global Cartesian coordinate system with the unit basis vectors $\boldsymbol{i}$ and $\boldsymbol{j}$. The local basis vectors $\boldsymbol{e}_{1,2}(s)$, which rotate with a particle, are introduced through the following geometric relations:

$$\boldsymbol{e}_1 = \cos\theta\,\boldsymbol{i} + \sin\theta\,\boldsymbol{j}, \quad \boldsymbol{e}_2 = -\sin\theta\,\boldsymbol{i} + \cos\theta\,\boldsymbol{j}, \tag{2}$$

in which θ denotes the rotation angle between the unit vector $\boldsymbol{e}_1$ and the axis x. We assume the undeformed reference configuration to be straight with $x = s$ and $\theta = 0$.

We decompose the angle of rotation of a particle into two parts:

$$\theta = \alpha + \psi, \quad \tan\alpha = \frac{y'}{x'} \tag{3}$$

with $\square'$ denoting a derivative with respect to s. The angle α measures the orientation of the tangent $\boldsymbol{r}'$ with respect to the x axis with respective unit tangent and normal vectors

$$\boldsymbol{t} = \cos\alpha\,\boldsymbol{i} + \sin\alpha\,\boldsymbol{j}, \quad \boldsymbol{n} = -\sin\alpha\,\boldsymbol{i} + \cos\alpha\,\boldsymbol{j}, \quad \partial_\alpha \boldsymbol{t} = \boldsymbol{n}, \quad \partial_\alpha \boldsymbol{n} = -\boldsymbol{t}. \tag{4}$$

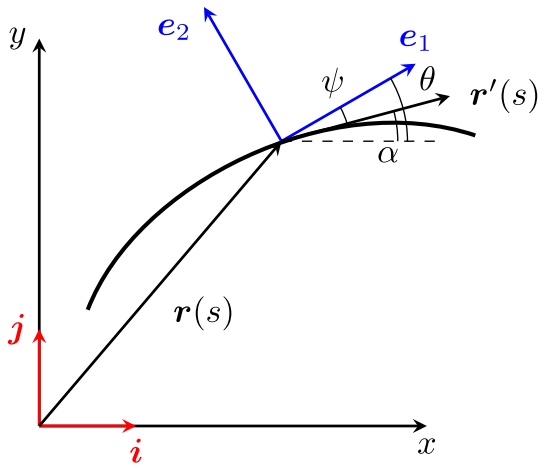

Fig. 1 Deformed rod configuration: centerline $\boldsymbol{r}(s)$ and local basis $\boldsymbol{e}_{1,2}(s)$ defined by the rotation angle θ

The additional rotation of a particle of the material line (which can be associated with the rotation of a cross-section) due to shear in (3) is denoted as ψ. The bending strain measure is the rate of rotation of a particle given as [5,20]

$$\kappa = \theta', \tag{5}$$

We define the axial strain ε and the shear strain γ as follows:

$$\varepsilon = \boldsymbol{e}_1 \cdot \boldsymbol{r}' - 1 = x' \cos\theta + y' \sin\theta - 1, \tag{6}$$

$$\gamma = \boldsymbol{e}_2 \cdot \boldsymbol{r}' = -x' \sin\theta + y' \cos\theta. \tag{7}$$

At static equilibrium the total energy of a rod, consisting of the total strain energy U^{strain} and the potential of external forces U^{ext}, obtains a minimum value with respect to the three unknown functions:

$$U^{\Sigma}[x(s),\ y(s),\ \theta(s)] = U^{\text{strain}} + U^{\text{ext}} \ \longrightarrow\ \min \tag{8}$$

In the present study, only stable equilibria are considered. The strain energy density is approximated by a quadratic form, and

$$U^{\text{strain}} = \int_0^L \frac{1}{2}\Big(a\,\kappa^2 + b\,\varepsilon^2 + c\,\gamma^2\Big)\,ds, \tag{9}$$

where a, b, and c represent the stiffness coefficients for bending, extension and shear, respectively. These coefficients are calculated as

$$a = EJ, \quad b = EA, \quad c = kGA, \quad G = \frac{E}{2(1+\nu)} \tag{10}$$

with E denoting Young's modulus, A area, J moment of inertia, G shear modulus and k shear correction factor of the cross section.

The presented formulation corresponds to what is commonly known as Timoshenko theory, while some evidence has recently been provided concerning the contribution of Ehrenfest to this formulation [40]. Next, we consider the extensible Bernoulli-Euler theory, in which the shear deformability is constrained by setting $\psi(s) = 0$, leading to γ vanishing identically. This constraint also ensures that the first basis vector coincides with the tangential direction to the centerline: $\boldsymbol{e}_1 = \boldsymbol{t}, \boldsymbol{e}_2 = \boldsymbol{n}, \boldsymbol{r}' = (1+\varepsilon)\boldsymbol{t}$. Consequently, the bending strain measure becomes the material curvature of the deformed axis of the rod:

$$\kappa = \alpha' = \frac{y''x' - x''y'}{|\boldsymbol{r}'|^2}, \tag{11}$$

and the axial strain takes the form

$$\varepsilon = |\boldsymbol{r}'| - 1, \tag{12}$$

which is known as the Biot strain measure. The minimization problem now involves two unknown functions, $x(s)$ and $y(s)$, with the strain energy given by

$$U^{\Sigma}[x(s),\ y(s)] \longrightarrow \min, \quad U^{\text{strain}} = \int_0^L \frac{1}{2}\Big(a\,\kappa^2 + b\,\varepsilon^2\Big)\,ds. \tag{13}$$

3 Model with independent shear approximation

In the present research, we aim to parametrize the additional rotation due to shear ψ instead of the rotation angle θ, as is usually done in the Timoshenko formulation. Additionally to being locking-free, the advantage of such a formulation is the smallness of ψ, which is expected to make handling additional effects due to shearability on top of a known Bernoulli-Euler solution more efficient.

Substituting the relation (3) into equation (5) we obtain the bending strain measure to

$$\kappa = \alpha' + \psi'. \tag{14}$$

Given that $\psi \ll 1$, which is the case when shear deformability is not pronounced, we keep just linear terms in

$$\sin\theta = \sin\alpha + \psi\cos\alpha, \quad \cos\theta = \cos\alpha - \psi\sin\alpha. \tag{15}$$

The axial strain (6) is now expressed as

$$\varepsilon = x'\cos\alpha - \cancel{x'\psi\sin\alpha} + y'\sin\alpha + \cancel{y'\psi\cos\alpha} - 1 = |\boldsymbol{r}'| - 1, \tag{16}$$

the terms with ψ cancel out because of (3). The axial strain thus coincides with the expression obtained in the Bernoulli-Euler theory (12). In a similar manner, the shear strain results into

$$\begin{aligned}\gamma = &\cancel{-x'\sin\alpha} - x'\psi\cos\alpha + \cancel{y'\cos\alpha} - y'\psi\sin\alpha = \\ &-\psi(x'\cos\alpha + y'\sin\alpha) = -\psi\boldsymbol{t}\cdot\boldsymbol{r}' = -\psi\,|\boldsymbol{r}'| = -\psi\sqrt{x'^2 + y'^2}.\end{aligned} \tag{17}$$

For the present case, the problem is solved by minimizing the total energy in terms of the independent field variables $x(s)$, $y(s)$ and $\psi(s)$:

$$U^{\Sigma}[x(s),\ y(s),\ \psi(s)] \longrightarrow \min, \quad U^{\text{strain}} = \int_0^L \frac{1}{2}\Big(a\,\kappa^2 + b\,\varepsilon^2 + c\,\gamma^2\Big)\,ds. \tag{18}$$

In the following, we refer to the problem (18) as *independent shear* model.

Using appropriate approximation of the independent functions $x(s)$, $y(s)$ and $\theta(s)$ (or $\psi(s)$), we treat the variational problems (8), (13) and (18) using a Newton iterative algorithm, in which the functional is approximated by a quadratic Taylor expansion around the current estimate. Starting from a reference state, a new estimate is obtained at each iteration by updating the previous one and the process is repeated until the updates fall below the prescribed tolerance.

The basic idea behind the approach with independent shear approximation is to solve the problem in two steps. First, a computationally more efficient model based on the Bernoulli–Euler theory is employed. The shear deformability is constrained by setting $\psi = 0$. After the problem is solved using the Newton iterative algorithm, we perform additional iterations, in which the shear deformability is added to the model in a correction step by allowing $\psi(s) \neq 0$. In the absence of essential nonlinearities, the correction step may be accomplished by solving just a single linear system of equations.

4 Incremental formulation

Within this novel approach, we further develop the idea of efficiently treating the effects of shear deformability on top of a known solution of the geometrically nonlinear formulation with constrained shear. After releasing the constraint $\gamma = 0$, the state changes slightly in the vicinity of this solution, which we use to the advantage of the numerical formulation. The respective increments are denoted by a dot as in $\dot{\square}$ and treated as infinitesimal, thus resulting into a linear perturbed problem with displacements on top of the Bernoulli-Euler solution. The displacements are expressed as

$$\dot{\boldsymbol{r}} = \boldsymbol{u} = u_x(s)\,\boldsymbol{i} + u_y(s)\,\boldsymbol{j}. \tag{19}$$

We introduce the $\bar{\square}$ notation to indicate the quantities derived from the Bernoulli-Euler solution. Accordingly, the current position vector reads

$$\boldsymbol{r} = \bar{\boldsymbol{r}} + \dot{\boldsymbol{r}} = \bar{\boldsymbol{r}} + \boldsymbol{u}; \tag{20}$$

the same decomposition applies to other variables. The unit normal remains orthogonal to the centerline, which results into an additional rotation of the unit normal and of the tangent to the centerline $\dot{\alpha}$:

$$\begin{aligned} &\boldsymbol{r}' \cdot \boldsymbol{n} = 0 \quad \Rightarrow \quad (\boldsymbol{r}' \cdot \boldsymbol{n})^{\cdot} = \boldsymbol{u}' \cdot \bar{\boldsymbol{n}} + \bar{\boldsymbol{r}}' \cdot \dot{\boldsymbol{n}} = 0, \\ &\dot{\boldsymbol{n}} = \dot{\alpha}\,\partial_\alpha \bar{\boldsymbol{n}} = -\dot{\alpha}\,\bar{\boldsymbol{t}} \quad \Rightarrow \quad \boldsymbol{u}' \cdot \bar{\boldsymbol{n}} = \dot{\alpha}\,\underbrace{\bar{\boldsymbol{r}}' \cdot \bar{\boldsymbol{t}}}_{=1+\bar{\varepsilon}} \quad \Rightarrow \quad \dot{\alpha} = \frac{\boldsymbol{u}' \cdot \bar{\boldsymbol{n}}}{1+\bar{\varepsilon}}. \end{aligned} \tag{21}$$

The total angle of rotation of the particle now equals the total angle of the rotation of the centerline plus the additional rotation because of shear:

$$\theta = \bar{\alpha} + \dot{\alpha} + \psi. \tag{22}$$

Numerical experiments below demonstrate the necessity to preserve at least quadratic terms in the increment of the axial strain measure because of the potentially high tensile force in the Bernoulli-Euler solution, which would otherwise discard some quadratic terms in the energy expression and the important geometric stiffening effect. The total axial strain, containing additional linear $\dot{\varepsilon}$ and quadratic $\ddot{\varepsilon}$ terms is computed as follows:

$$\varepsilon = \bar{\varepsilon} + \dot{\varepsilon} + \ddot{\varepsilon} = (\bar{\boldsymbol{r}}' + \boldsymbol{u}') \cdot \boldsymbol{e}_1 - 1; \tag{23}$$

note that the above expression is exact. We keep terms up to the second order of smallness in the series expansion of the local basis vector $\boldsymbol{e}_1$:

$$\begin{aligned} \boldsymbol{e}_1 &= \cos(\bar{\alpha} + \dot{\alpha} + \psi)\,\boldsymbol{i} + \sin(\bar{\alpha} + \dot{\alpha} + \psi)\,\boldsymbol{j} = \\ &= \bar{\boldsymbol{t}} + (\dot{\alpha} + \psi)\,\bar{\boldsymbol{n}} - \frac{1}{2}(\dot{\alpha} + \psi)^2\,\bar{\boldsymbol{t}} + \cdots \end{aligned} \tag{24}$$

with $(\cdots)$ denoting terms of higher order of smallness. By substituting the expression (24) into (23) we find

$$\begin{aligned} \varepsilon &= \underbrace{\bar{\boldsymbol{r}}' \cdot \bar{\boldsymbol{t}} - 1}_{=\bar{\varepsilon}} - \tfrac{1}{2}(\dot{\alpha} + \psi)^2\,\underbrace{\bar{\boldsymbol{r}}' \cdot \bar{\boldsymbol{t}}}_{=1+\bar{\varepsilon}} + \boldsymbol{u}' \cdot \bar{\boldsymbol{t}} + (\dot{\alpha} + \psi)\,\boldsymbol{u}' \cdot \bar{\boldsymbol{n}} + \cdots \\ \Rightarrow \quad &\dot{\varepsilon} = \boldsymbol{u}' \cdot \bar{\boldsymbol{t}}, \quad \ddot{\varepsilon} = (\dot{\alpha} + \psi)\,\boldsymbol{u}' \cdot \bar{\boldsymbol{n}} - \frac{1}{2}(\dot{\alpha} + \psi)^2\,(1 + \bar{\varepsilon}). \end{aligned} \tag{25}$$

Since there was no shear in the unperturbed state, the total shear equals the increment

$$\gamma = \dot{\gamma} = (\bar{\boldsymbol{r}} + \boldsymbol{u})' \cdot \boldsymbol{e}_2, \tag{26}$$

where $\boldsymbol{e}_2$ is given as

$$\boldsymbol{e}_2 = \bar{\boldsymbol{n}} - (\dot{\alpha} + \psi)\,\bar{\boldsymbol{t}} + \cdots. \tag{27}$$

Taking the previous relation into account, using equation (21), and neglecting quadratic and higher order terms, the total shear can be expressed as follows:

$$\gamma = \boldsymbol{u}' \cdot \bar{\boldsymbol{n}} - (\dot{\alpha} + \psi)\,\underbrace{\bar{\boldsymbol{r}}' \cdot \bar{\boldsymbol{t}}}_{=1+\bar{\varepsilon}} + \cdots \quad \Rightarrow \quad \dot{\gamma} = -\psi(1 + \bar{\varepsilon}). \tag{28}$$

Table 1 Summary of approximated fields for different models

Model	NURBS approximation of unknown functions
Bernoulli–Euler	$x(\xi) = \sum_{i=1}^{N_{cp}} R_{i,p}(\xi)\, x_i, \quad y(\xi) = \sum_{i=1}^{N_{cp}} R_{i,p}(\xi)\, y_i$
Timoshenko	$x(\xi) = \sum_{i=1}^{N_{cp}} R_{i,p}(\xi)\, x_i, \quad y(\xi) = \sum_{i=1}^{N_{cp}} R_{i,p}(\xi)\, y_i, \theta(\xi) = \sum_{i=1}^{N_{cp}} R_{i,p}(\xi)\, \theta_i$
Independent shear	$x(\xi) = \sum_{i=1}^{N_{cp}} R_{i,p}(\xi)\, x_i, \quad y(\xi) = \sum_{i=1}^{N_{cp}} R_{i,p}(\xi)\, y_i, \psi(\xi) = \sum_{i=1}^{N_{cp}} R_{i,p}(\xi)\, \psi_i$
Incremental	$u_x(\xi) = \sum_{i=1}^{N_{cp}} R_{i,p}(\xi)\, u_{xi}, \quad u_y(\xi) = \sum_{i=1}^{N_{cp}} R_{i,p}(\xi)\, u_{yi}, \psi(\xi) = \sum_{i=1}^{N_{cp}} R_{i,p}(\xi)\, \psi_i$

The curvature is now defined as

$$\kappa = \bar{\alpha}' + \dot{\alpha}' + \psi'. \tag{29}$$

The presented *incremental model* features minimization of the total energy of a rod in the perturbed state performed with respect to the following unknown functions:

$$U^{\Sigma}[u_x(s),\ u_y(s),\ \psi(s)] \ \longrightarrow\ \min. \tag{30}$$

The total strain energy is given by the below integral, in which terms up to the second order are preserved in ε^2:

$$\begin{aligned} U^{\text{strain}} &= \int_0^L \frac{1}{2}\Big(a\,\kappa^2 + b\,\varepsilon^2 + c\,\gamma^2\Big)\,ds, \\ \varepsilon^2 &= \bar{\varepsilon}^2 + 2\bar{\varepsilon}\dot{\varepsilon} + 2\bar{\varepsilon}\ddot{\varepsilon} + \dot{\varepsilon}^2. \end{aligned} \tag{31}$$

5 NURBS approximation

In the simulations below the unknown functions are approximated using Non-Uniform Rational B-spline (NURBS) basis functions, within the framework of isogeometric analysis (IGA). A NURBS curve of order p is defined by

$$\boldsymbol{r}(\xi) = \sum_{i=1}^{N_{cp}} R_{i,p}(\xi)\, \boldsymbol{P}_i, \quad R_{i,p}(\xi) = \frac{B_{i,p}(\xi)\, w_i}{\sum_{j=1}^{N_{cp}} B_{j,p}(\xi)\, w_j}, \tag{32}$$

where $B_{i,p}(\xi)$ are B-spline basis functions, $\boldsymbol{P}_i$ are the control points, $R_{i,p}(\xi)$ are rational basis functions, w_i are weights associated with i^{th} control point, and N_{cp} is the number of control points. The parameter $\xi \in [0, 1]$ represents the non-dimensional coordinate related to the material coordinate s through the mapping $\xi = \xi(s)$. Hence, derivatives with respect to the material coordinate are obtained through

$$\frac{\partial \square}{\partial s} = \frac{\partial \square}{\partial \xi}\frac{\partial \xi}{\partial s}. \tag{33}$$

The parameter space [0, 1] is partitioned according to the knot vector $\boldsymbol{\xi} = \{0 = \xi_1,\ \xi_2, \cdots,\ \xi_{N_{cp}+p},\ \xi_{N_{cp}+p+1} = 1\}$, a set of non-decreasing sequence of real numbers, called knots. In this paper, only open knot vectors are employed and each non-zero knot span (ξ_i, ξ_{i+1}) defines a single isogeometric finite element. The interelement continuity of the basis functions is C^{p-1} at maximum and can be decreased by repeating the same knot value. For an in-depth discussion we refer to [27] and [41].

Once the reference geometry is exactly represented using NURBS, the unknown fields are approximated with the same basis functions. Table 1 provides an overview of the four models, indicating the choice of control variables $(x_i,\ y_i,\ u_{xi},\ u_{yi},\ \theta_i,\ \psi_i)$ in each case.

There are many studies that address the optimal quadrature rule in IGA, for example [42] and [43]. In the present research, the numerical integration of the total energy is performed at the element level using the Gaussian quadrature rule with $p + 1$ integration points. This number is adopted for all computations in the paper, while a detailed analysis of its influence will be carried out in future research.

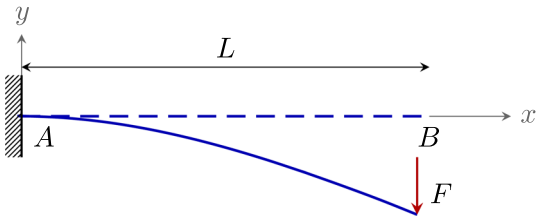

Fig. 2 Benchmark example: rod under point force

Table 2 Reference solutions for different values of the applied force

	x_B	y_B	θ_B	ε_B	κ_A	γ_A
$F = 10^5$	0.95156	−0.28045	−0.4268	0.00007	−0.87	−0.00059
$F = 7 \cdot 10^5$	0.54875	−0.7565	−1.3051	0.00129	−3.51197	−0.00416

6 Numerical validation: rod under point force

We begin validating the developed approaches by considering a simple example involving a one-dimensional rod with a constant square cross section under the transverse end load F, as depicted in Fig. 2. The parameters of the example used for the investigation are expressed in SI units as follows: $L = 1$, $E = 2.1 \cdot 10^{11}$, $\nu = 0.3$, $k = 5/6$. The width and the height of the cross-section is 0.05. The results are presented for representative locations, denoted as points A and B, which correspond to the left and right ends of a rod, respectively.

The reference solution is derived from equilibrium equations of the nonlinear theory of shear-deformable rods [6], given in general form as

$$\boldsymbol{Q}' + \boldsymbol{q} = \boldsymbol{0}, \quad M' + \boldsymbol{r}' \times \boldsymbol{Q} \cdot \boldsymbol{k} + m = 0, \tag{34}$$

where $\boldsymbol{Q}$ is the internal force vector, M the bending moment, $\boldsymbol{k}$ is the out of plane unit vector and $\boldsymbol{q}$ and m are the external distributed forces and moments, respectively For the given example, the internal force is constant because of $\boldsymbol{q} = \boldsymbol{0}$ and it is known from the boundary condition: $\boldsymbol{Q} = -F\boldsymbol{e}_y$. Denoting the axial force with Q_1 and the shear force with Q_2, we use the constitutive equations as $\varepsilon = Q_1/b$, $\gamma = Q_2/c$, and obtain the vector $\boldsymbol{r}'$ from the kinematic relations (6), (7):

$$\begin{aligned} \boldsymbol{r}' &= (b^{-1}Q_1 + 1)\boldsymbol{e}_1 + c^{-1}Q_2\boldsymbol{e}_2, \\ Q_1 &= -F\sin\theta, \quad Q_2 = -F\cos\theta. \end{aligned} \tag{35}$$

We use these relations, balance of moments as the second equation of (5), the further elastic relation $M = a\kappa = a\theta'$ and the transformed mixed product

$$\boldsymbol{r}' \times \boldsymbol{Q} \cdot \boldsymbol{k} = (b^{-1}Q_1 + 1)Q_2 - c^{-1}Q_2Q_1, \tag{36}$$

which leads us to the single differential equation for the angle of rotation

$$a\theta'' - F\cos\theta + F^2\cos\theta\sin\theta(b^{-1} - c^{-1}) = 0. \tag{37}$$

Along with the boundary conditions $\theta(0) = 0$ and $\theta'(L) = 0$ (the bending moment vanishes at the free end), we face a necessity to solve a nonlinear BVP, for which we use the shooting method implemented in Wolfram Mathematica.[1] The obtained reference solutions for strains and displacements at representative locations, under different values of the applied force, are presented in Table 2.

The numerical results are computed using 50 quartic isogeometric elements with C^1 continuity, which is chosen with respect to the further application to contact, as explained in more detail in Sect. 8 after (46). The relative errors ϵ with respect to the reference solutions, are reported in Tables 3 and 4. It is of particular interest that for both, the Incremental and Independent shear model, the results were obtained with a single Newton iteration on top of a converged Bernoulli-Euler solution. Furthermore, results with the Independent

[1] https://www.wolfram.com/mathematica.

Table 3 Relative differences compared to the analytical solution: $F = 10^5$

	Bernoulli-Euler	Timoshenko	Independent shear-single it.	Independent shear-multiple it.	Incremental
ϵ_{x_B}	0.00015	$1.53 \cdot 10^{-9}$	$9.74 \cdot 10^{-8}$	$1.2 \cdot 10^{-7}$	$1.68 \cdot 10^{-8}$
ϵ_{y_B}	0.00175	$1.9 \cdot 10^{-8}$	$1.3 \cdot 10^{-7}$	$5.44 \cdot 10^{-7}$	$1.89 \cdot 10^{-8}$
ϵ_{θ_B}	0.00018	$2.28 \cdot 10^{-8}$	$1.2 \cdot 10^{-7}$	$7.3 \cdot 10^{-8}$	$3.93 \cdot 10^{-9}$
ϵ_{ε_B}	0.00017	$2.53 \cdot 10^{-6}$	0.00256	$2.59 \cdot 10^{-6}$	0.00032
ϵ_{κ_A}	0.00015	$8.06 \cdot 10^{-9}$	$3.17 \cdot 10^{-8}$	$1.21 \cdot 10^{-7}$	$1.89 \cdot 10^{-8}$
ϵ_{γ_A}	–	$7.59 \cdot 10^{-7}$	$6.85 \cdot 10^{-7}$	$2.08 \cdot 10^{-6}$	$2.4 \cdot 10^{-5}$

Table 4 Relative differences compared to the analytical soluton: $F = 7 \cdot 10^5$

	Bernoulli-Euler	Timoshenko	Independent shear-single it.	Independent shear-multiple it.	Incremental
ϵ_{x_B}	0.00117	$5.07 \cdot 10^{-8}$	$4.31 \cdot 10^{-6}$	$1.69 \cdot 10^{-7}$	$5.75 \cdot 10^{-7}$
ϵ_{y_B}	0.00139	$1.35 \cdot 10^{-8}$	$2.21 \cdot 10^{-6}$	$5.34 \cdot 10^{-6}$	$8.91 \cdot 10^{-7}$
ϵ_{θ_B}	0.0009	$8.19 \cdot 10^{-8}$	$3.49 \cdot 10^{-6}$	$2.96 \cdot 10^{-6}$	$8.76 \cdot 10^{-8}$
ϵ_{ε_B}	0.00033	$1.54 \cdot 10^{-6}$	0.0003	$3.15 \cdot 10^{-6}$	0.00013
ϵ_{κ_A}	0.00119	$8.42 \cdot 10^{-8}$	$6.64 \cdot 10^{-7}$	$7.52 \cdot 10^{-7}$	$9.1 \cdot 10^{-9}$
ϵ_{γ_A}	–	$2.99 \cdot 10^{-5}$	$1.91 \cdot 10^{-5}$	$8 \cdot 10^{-5}$	0

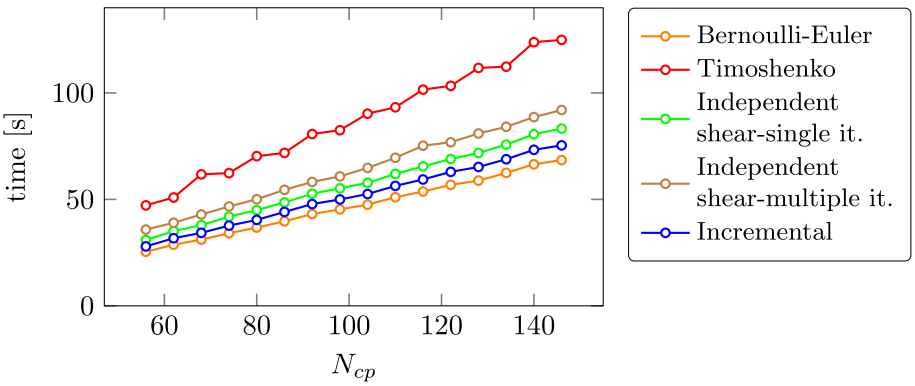

Fig. 3 Rod under a point force—computation time

shear model calculated by performing a full Newton minimization starting from the initial configuration are also presented for comparison.

For both values of the external force we observe a good correspondence with the reference semi-analytical solution, demonstrating the applicability of novel approaches even at significant deformations, with only minor differences compared to the classical shear-deformable model. The Independent shear model performed in a single step achieves relative errors comparable to those obtained with full Newton minimization, showing the effectiveness of a single-step update. The higher relative errors in the axial strain for the smaller value of F are because ε_B is very small in the reference solution. Performing multiple Newton iterations could further decrease the error.

The computational efficiency of the models is compared in Fig. 3, where the total time required for each model is plotted as a function of the number of control points for the higher value of the applied force. It is performed by varying the number of elements N_{el} using cubic polynomials with C^1 interelement continuity. The results show that the novel approaches enhance efficiency by reducing the computational cost, while maintaining accuracy. The relatively high absolute values of the computation time are due to the current non-optimized implementation of the Newton method using Wolfram Mathematica.

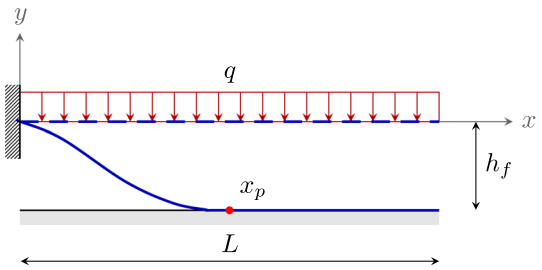

Fig. 4 Benchmark exapmple: rod under distributed load in contact with a rigid foundation

7 Approach to contact problems

Computational contact mechanics offers a range of numerical methods for modeling interactions between solid bodies in contact conditions [10]. In this study, we focus on the contact of a rod with rigid surfaces under the simplified assumption of frictionless interaction. For this sake we employ the penalty method using the contact potential U^{con}, which penalizes the penetration of the rod into the surface. The minimization problem takes now the form

$$U^{\Sigma} = U^{\text{strain}} + U^{\text{ext}} + U^{\text{con}} \longrightarrow \min . \tag{38}$$

The contact potential is an integral over the potential contact domain c:

$$U^{\text{con}} = \int_c \frac{1}{2}\mathbb{C}\max(0, g)^2 \, ds. \tag{39}$$

Here, $\mathbb{C}$ denotes the penalty parameter, and g represents the gap function, which is the penetration depth in the contact zone and which becomes negative if there is no contact at a specific location. The impenetrability condition is satisfied only in the limit as $\mathbb{C} \to \infty$. On the other hand, increasing the penalty parameter leads to an ill-conditioned numerical minimization problem, which can be overcome by employing the augmented Lagrangian method [44]. The idea behind is to enhance the contact potential by a linear term with the Lagrange multiplier $\lambda(s)$ being an estimate for the correct value of the contact pressure:

$$U^{\text{con}} = \int_c \left(\frac{1}{2}\mathbb{C}\max(0, g)^2 + \lambda g\right) ds, \tag{40}$$

while the Lagrange multipliers are iteratively updated according to

$$\lambda^{k+1} = \max(0, \ \lambda^k + \mathbb{C}g). \tag{41}$$

Importantly, this update scheme does not immediately set the value of λ at a specific integration point to zero if the contact gets lost with $g < 0$, but merely reduces its current value, which regularizes the convergence of iterations. The penetration depth turns into zero in the entire contact zone as soon as $\lambda(s)$ is exact.

8 Contact with a straight foundation

To test the derived approaches for contact problems, we first consider a rod from the previous example, subjected to a distributed load $q = 10^6$, with a problem setup shown in Fig. 4. The rod deforms, and comes into contact with a straight foundation, which is considered rigid at a depth of $h_f = 0.01$ below the rod. The boundary between the contact and non-contact regions is denoted by x_p, which we call transition point.

For the present case, the gap function is defined as

$$g = -y - h_f. \tag{42}$$

Given the small foundation depth, we compared the results against the analytical solution for the geometrically linear Timoshenko beam model, for which the local basis $\boldsymbol{e}_1$ and $\boldsymbol{e}_2$ remain identical, with $\boldsymbol{e}_1 = \boldsymbol{e}_x$ and $\boldsymbol{e}_2 = \boldsymbol{e}_y$. To derive this reference solution, we first consider the segment with no contact $s < x_p$. According to the linear

counterpart of the balance equations (34), here the transverse shear force is changing linearly and thus the bending moment is a quadratic function of s:

$$\begin{aligned} \boldsymbol{Q}' - q\boldsymbol{e}_y = \boldsymbol{0} \;\; &\Rightarrow \;\; Q_2 = qs + C_1, \\ M' + Q = 0 \;\; &\Rightarrow \;\; M = -q\frac{s^2}{2} - C_1 s + C_2. \end{aligned} \tag{43}$$

Here, C_1 and C_2 are the unknown integration constants. The constitutive relations from Sect. 6 simplify to $M = a\theta'$ and $Q_2 = c(y' - \theta)$. Integrating, we find the rotation of particles and the deflection of the centerline of the rod:

$$\begin{aligned} \theta &= a^{-1}\left(-q\tfrac{s^3}{6} - C_1\tfrac{s^2}{2} + C_2 s + C_3\right), \\ y &= a^{-1}\left(-q\frac{s^4}{24} - C_1\frac{s^3}{6} + C_2\frac{s^2}{2} + C_3 s\right) + c^{-1}\left(q\frac{s^2}{2} + C_1 s\right) + C_4 \end{aligned} \tag{44}$$

with C_3 and C_4 being further integration constants.

In the contact segment $s \geq x_p$ the deflection $y = -h_f$ is constant, which means the shear force is proportional to the rotation: $Q_2 = -c\theta$. Along with the elastic relation for the bending moment and absence of distributed moment interaction, this results into the following equation of balance of moment:

$$a\theta'' - c\theta = 0 \;\; \Rightarrow \;\; \theta = C_5 e^{-\sqrt{cs/a}} + C_6 e^{\sqrt{cs/a}}. \tag{45}$$

Given that $\theta(\infty) = 0$ in the contact zone, we conclude that C_6 must vanish, so the problem reduces to solving a system of 6 equations with 5 unknown integration constants and the unknown position of the transition point x_p. The mentioned equations feature the boundary conditions $y^{(1)} = 0$, $\theta^{(1)} = 0$ at $s = 0$ as well as the transition conditions: $y^{(1)} = -h_f$, $Q_2^{(1)} = Q_2^{(2)}$, $M^{(1)} = M^{(2)}$, $\theta^{(1)} = \theta^{(2)}$ at $s = x_p$. Here, $(\cdots)^{(1)}$ and $(\cdots)^{(2)}$ indicate quantities associated with the non-contact and contact segments, respectively. We solve the equations, which are nonlinear in terms of x_p, with the help of Wolfram Mathematica and compute the contact pressure in $x \geq x_p$ according to

$$p_c = q - Q_2'. \tag{46}$$

In the remainder of this section we use the obtained analytical solution to validate the numerical results for all the models introduced above. We begin the comparison by using a fine discretization of 55 quartic elements with C^1 continuity and a uniform knot vector, with the motivation for this choice of continuity level being twofold: the fourth order approximation should be able to accurately represent the solution in the free segment $s < x_p$ and in the contact one $x > x_p$ providing rapid convergence, while the reduced inter-element continuity is expected to efficiently handle the discontinuous contact pressure p_c in the transition point $x = x_p$. In Fig. 5 we plot the pressure distributions in the middle part of the rod for different values of the penalty parameter.

It should be noted, that for Incremental and Independent shear model, multiple Newton iterations were performed on top of the Bernoulli-Euler solution as required to resolve the essential nonlinearity due to contact. For the Bernoulli-Euler model we see that increasing the penalty parameter leads to the formation of pronounced peaks near the contact boundary, while in the rest of the contact region the pressure remains constant. This behavior is consistent with the semi-analytical treatments of similar problems predicting concentrated reactions in the transition point in the absence of shear [15,20]. For lower values of the penalty parameter, all shear-deformable models produce nearly identical contact force distributions. As the penalty parameter increases, oscillations in the vicinity of the transition point appear and grow with similar intensity for all models, overestimating the maximum contact pressure. Note that according to the analytical solution, the transition point is located at $x_p = 0.5$ and the presented results with an odd number of elements correspond to the situation, where the contact zone boundary lies in the middle of an element, which explains the oscillatory behavior.

Next, we consider the case where the transition point coincides with the element boundary or is at least very close to it, and investigate the effect of the interelement continuity. Since increasing the continuity also reduces the number of control points, meshes with different even numbers of quartic elements, but with approximately equal number of control points are used. The adopted number of elements is $N_{el} = 54$ for C^1 continuity and $N_{el} = 80$ for C^2 continuity, while the penalty parameter is $\mathbb{C} = 5 \cdot 10^{13}$. The shear strain and the contact force distributions are shown in Fig. 6.

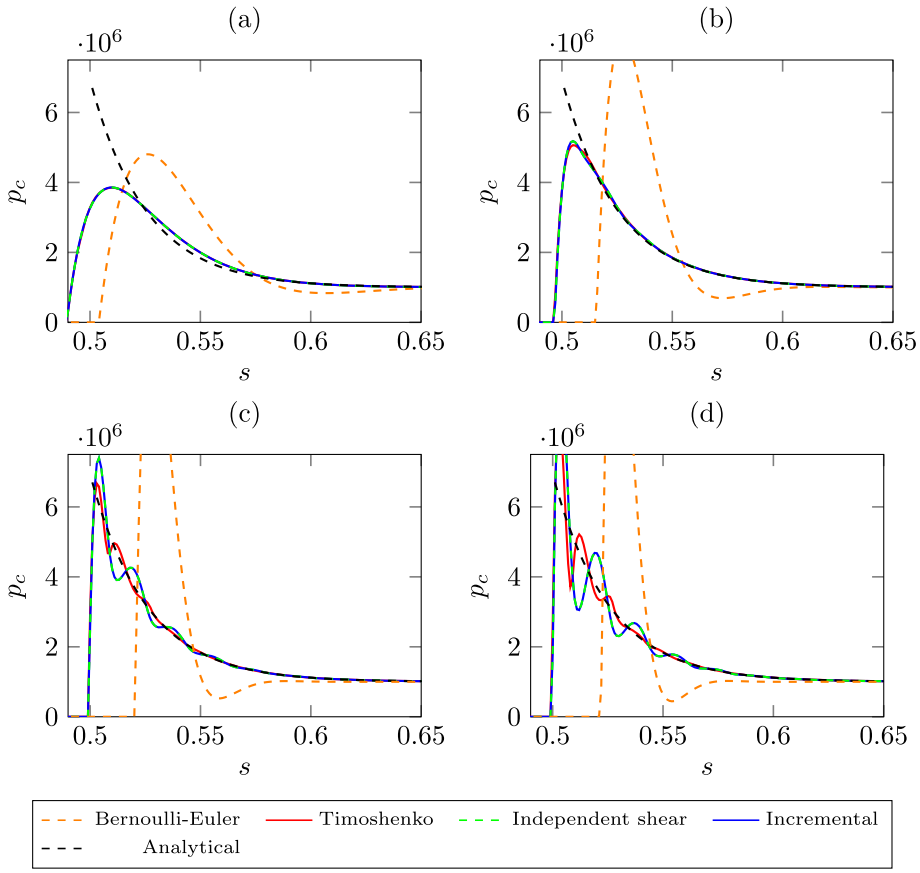

Fig. 5 Rod under distributed load with contact—contact pressure distributions for different penalty parameters: **(a)** $\mathbb{C} = 10^{12}$; **(b)** $\mathbb{C} = 10^{13}$; **(c)** $\mathbb{C} = 5 \cdot 10^{13}$; **(d)** $\mathbb{C} = 10^{14}$

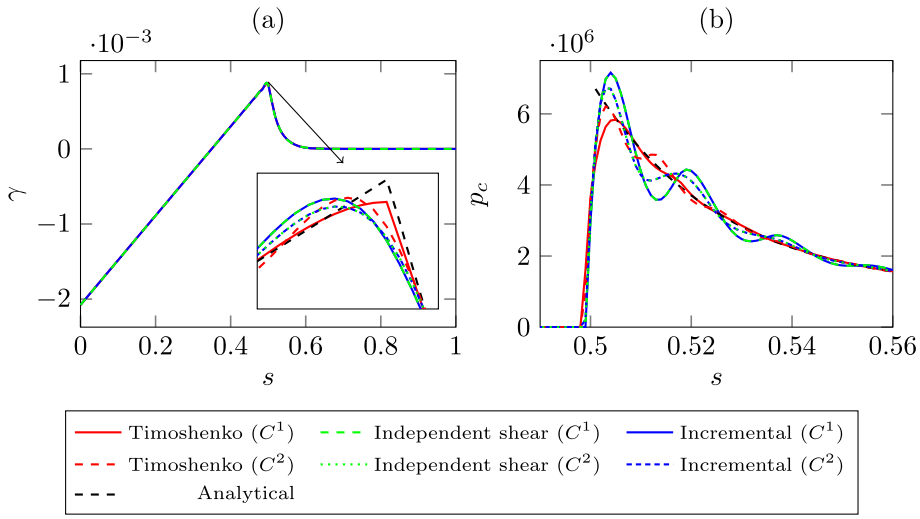

Fig. 6 Rod under distributed load with contact—different interelement continuity: **(a)** shear strain; **(b)** contact pressure distributions

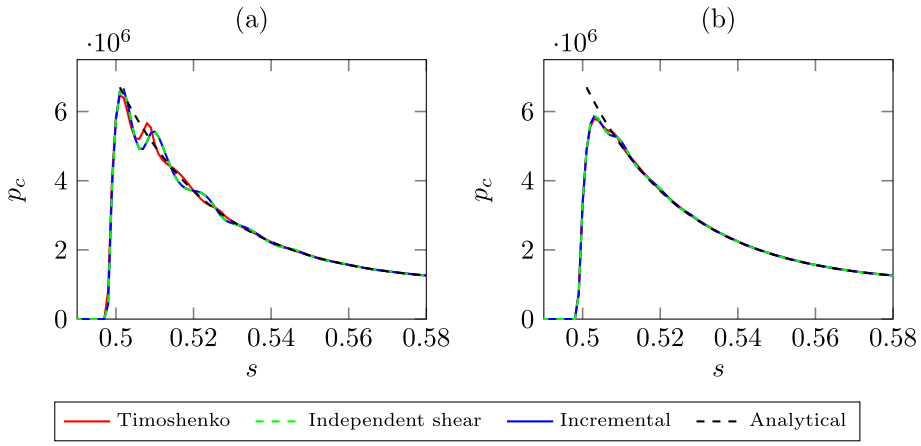

Fig. 7 Rod under distributed load with contact—contact pressure distributions for higher polynomial orders: **(a)** $p = 5$; **(b)** $p = 6$

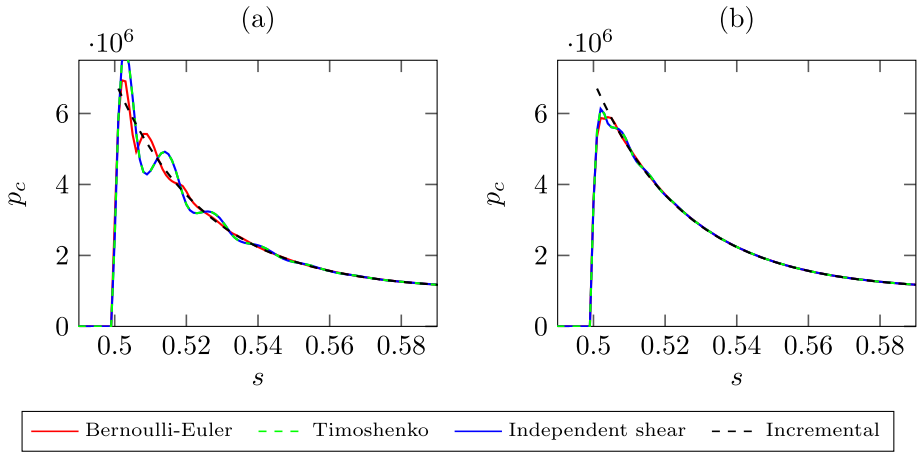

Fig. 8 Rod under distributed load with contact—contact pressure distributions for different numbers of elements: **(a)** $N_{el} = 75$; **(b)** $N_{el} = 135$

The numerical results remain in good agreement with the analytical solution. The shear strain exhibits a kink at the transition point, which cannot be accurately captured when using higher orders of continuity. On the other hand, higher continuity reduces the amplitude of the oscillations in contact pressure. The exception is the Timoshenko model, for which the loss of regularity can be approximated with C^1 interelement continuity, which explains smaller oscillations in the contact pressure in this case.

Several strategies help reducing the observed oscillations. One of the possibilities is to elevate the polynomial order p of the basis functions, which also leads to a higher number of control points. Returning to the general case when the transition point does not coincide with the element boundary, in Fig. 7 we display the contact pressure distributions obtained with a mesh with 55 quintic and sextic elements, with $\mathbb{C} = 5 \cdot 10^{13}$ and C^1 interelement continuity.

Comparing to the results obtained with quartic elements in Fig. 5c, we conclude that employing higher-order polynomials reduces the oscillations, which are almost negligible when sextic elements are used.

Another strategy we investigated is to use more elements, while keeping the polynomial order and continuity fixed. For this case, the penalty parameter was increased to $\mathbb{C} = 10^{14}$ and quartic elements with C^1 continuity are employed. The results, shown in Fig. 8, indicate that when mesh is sufficiently dense, all models exibit the same behaviour, which aligns well with the analytical solution.

Increasing the penalty parameter required a finer mesh, but also produced higher maximum pressure values. Regarding the strains, all models produce comparable results and match the analytical solution closely.

Next, we consider the Augmented Lagrangian method, using a mesh consisting of 65 quartic elements with C^1 continuity. The contact forces in Gauss points, obtained with a different penalty parameters and different number of iterations, are presented in Figs. 9 and 10. The required number of iterations depends on the chosen

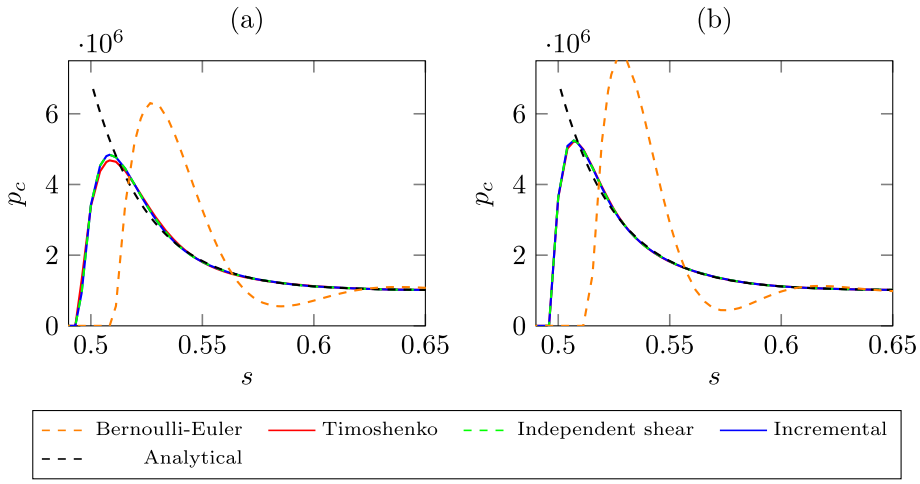

Fig. 9 Rod under distributed load with contact—augmented Lagrangian method with penalty parameter $\mathbb{C} = 7 \cdot 10^{10}$: **(a)** 50 iterations; **(b)** 100 iterations

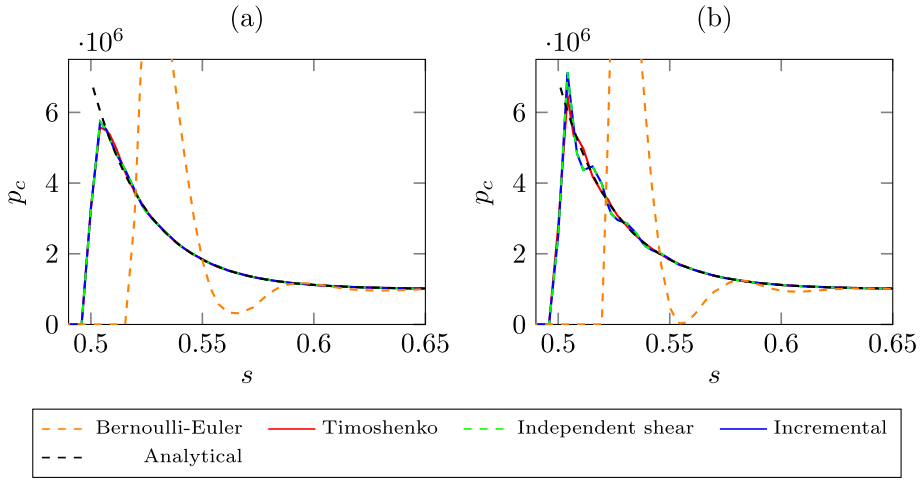

Fig. 10 Rod under distributed load with contact—augmented Lagrangian method with penalty parameter $\mathbb{C} = 7 \cdot 10^{11}$: **(a)** 50 iterations; **(b)** 100 iterations

penalty parameter, the higher values generally reduce the iteration count. However, if the penalty parameter is increased beyond an optimale range, oscillations may still occur.

The required computational times are illustrated in Fig. 11 for quartic elements with C^1 continuity and increasing the number of elements.

We again note that the current version of the code is not fully optimized, and the results are obtained using a Newton iteration tolerance of 10^{-10}. Comparing the computational effort needed for each model, we conclude that the novel approaches are more efficient than the classical Timoshenko model, which is especially pronounced when a higher number of control points is employed: just a few iterations are necessary on top of a converged solution with the Bernoulli-Euler model, which itself is also more efficient.

9 Formulation of the belt-pulley contact problem

We demonstrate the proposed methods on a less academic and more challenging example of a belt-pulley frictionless contact problem, investigated with the Bernoulli-Euler rod formulation in [15] and with the shear-deformable Timoshenko model in [20]. The set-up is displayed in Fig. 12.

Dashed lines depict the initial state, in which the belt is a circle of the radius a_0 and the pulleys (which are rigid disks of the radius a_1) are merely touching the belt. Note that the curvature and the respective bending

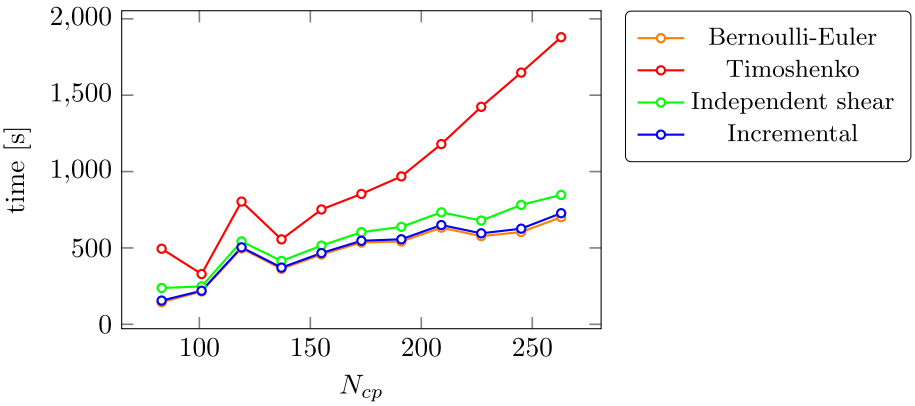

Fig. 11 Rod under distributed load with contact—computation time

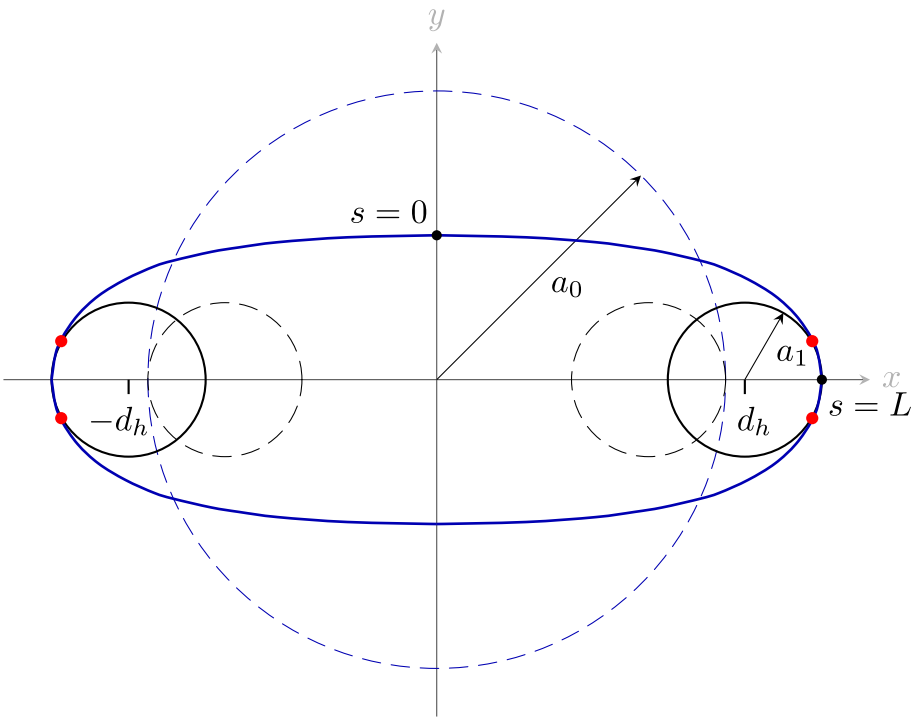

Fig. 12 Belt-pulley frictionless contact problem: moving the pulleys (black circles) away from each other, one deforms the belt (blue line) and the contact domains become continuous bounded by four transition points (red)

moment in this initial state have no influence on the solution as the set-up always resides in the xy plane. Indeed, identical behavior would have been obtained by considering the initial state stress-free with the natural curvature $\kappa_0 = -a_0^{-1}$, which is negative because of the direction of the arc-lengh coordinate s as $\theta'(s) < 0$.

Shifting the pulleys away from each other along the x axis, we deform the belt, and the contact segments grow to a finite length; their boundaries are transition points plotted by red dots. The coordinate of the center of the right pulley d_h is the kinematic load parameter. The major difference to the previously considered examples lies in the high tensile forces and essential axial strain induced by the kinematic loading. An analytical solution to the problem is available in [20] and will be used as a reference for validating the presented numerical schemes. We also refer to the analytical investigation in [45] featuring a geometrically linear model in a similar setting

From the previous research on the frictional contact problem of a moving belt and rotating pulley [16,17] we know that shear compliance plays not only a regularizing role helping to deal with distributed contact pressure and friction force instead of concentrated interactions in transition points. Moreover, it turns out to

Table 5 Relative errors of the axial strain and the curvature change at two specific locations; reference values are provided in the rightmost column

Variable	Timoshenko	Independent shear	Incremental	Analytical solution
ϵ_ε at $s = 0$	$4.38 \cdot 10^{-6}$	$4.51 \cdot 10^{-5}$	$9.45 \cdot 10^{-6}$	$\varepsilon = 0.001$
ϵ_κ at $s = 0$	$4.84 \cdot 10^{-7}$	$1.2 \cdot 10^{-5}$	$4.87 \cdot 10^{-6}$	$\kappa + a_0^{-1} = 3.43016$
ϵ_ε at $s = L$	$4.71 \cdot 10^{-7}$	$7.2 \cdot 10^{-5}$	$9.2 \cdot 10^{-6}$	$\varepsilon = 0.00058$
ϵ_κ at $s = L$	$7.98 \cdot 10^{-7}$	$1.22 \cdot 10^{-5}$	$1.18 \cdot 10^{-5}$	$\kappa + a_0^{-1} = -6.00584$

be essential for avoiding overdetermined systems of equations and thus render the problem solvable. Even more importantly, taking the shear deformability into account is essential from the physical point of view as it results into more realistic contact pressure distributions [13]. The present investigation aims at demonstrating the efficiency of the suggested kinematic models in the present context as well as the optimum approximation order and interelement continuity conditions.

Given that the problem has two axes of symmetry, we considered only the upper right quarter of belt, applying the corresponding symmetry boundary conditions at the crossing with the y axis where $s = 0$ and at the crossing with the x axis, where $s = L$. In accordance with [20], we choose the material parameters as follows: $E = 10^9$ and Poisson's ratio $\nu = 0.5$. In the initial state, the belt has a radius of $a_0 = 0.25$ corresponding to $L = 2\pi a_0/4 = 0.3927$, the pulley radius is $a_1 = 0.1$, while the belt has a square cross section of width and height 0.01. For the sake of simplicity, we impose the contact condition at the centerline of the rod. The pulleys are shifted apart from each other such that the distance between their centers becomes $2(a_0 - a_1) + \delta = 2d_h$, where δ denotes the imposed pulley displacement. According to the analytical solution, the end of the contact segment is located at $s = 0.3247$ when the pulley displacement equals $\delta = 0.159$.

10 Simulations of the belt-pulley contact

In this section, we present the computation results for the contact problem between the belt and the pulleys. The general workflow of the simulation is analogous to Sect. 8 with the gap function defined as

$$g = a_1 - |\boldsymbol{r} - d_h \boldsymbol{i}|. \tag{47}$$

We compared the numerical results with the analytical values of the axial strain and curvature change from the initial circular state $\kappa - \kappa_0 = \kappa + a_0^{-1}$ at $s = 0$ and $s = L$. The analytical values and corresponding relative errors are reported in Table 5. The computations were performed using an uniform knot vector with 100 quartic elements and C^1 interelement continuity.

The convergence behavior for axial strain and curvature change at $s = L$ is shown in Fig. 13. The results are obtained with cubic isogeometric finite elements with C^1 and C^2 interelement continuity and a penalty parameter $\mathbb{C} = 10^{11}$. The tolerance of the Newton loop was set to 10^{-13} in this case. It is observed that the Independent shear and Incremental models exhibit very similar convergence properties, and result into the relative errors close to those of the Timoshenko model. We notice that increased interelement continuity improves the accuracy of the axial strain (reduces ϵ_ε), while the curvature is more accurate with the C^1 continuity for the Independent shear and Incremental models. On the other hand, the classical Timoshenko solution benefits from the higher interelement continuity. In this context we also refer to the discussion of the effect of the interelement continuity on the contact pressure distribution in Fig. 6. Note that the convergence of different strains and forces at different locations may be different for the same model.

The contact forces, obtained with the 85 elements, and computed at the Gauss points for different values of penalty parameter are displayed in Fig. 14. Despite the fine discretization, the contact zone is small, with around 16 elements appearing in it, and therefore some oscillations are still observed, especially pronounced for the higher value of penalty parameter. To overcome this, we employ a non-uniform knot vector, with finer elements placed in the last quarter of the belt, while the number of elements is reduced in the remaining region. The contact segment now contains approximately 30 elements, while the total number of elements is 65. The element sizes vary, with the largest element being about five times the size of the smallest one. The contact force distribution and the shear strain for the penalty parameter $\mathbb{C} = 5 \cdot 10^{11}$ are shown in Fig. 15. The obtained results are in a very good agreement with the analytical solution.

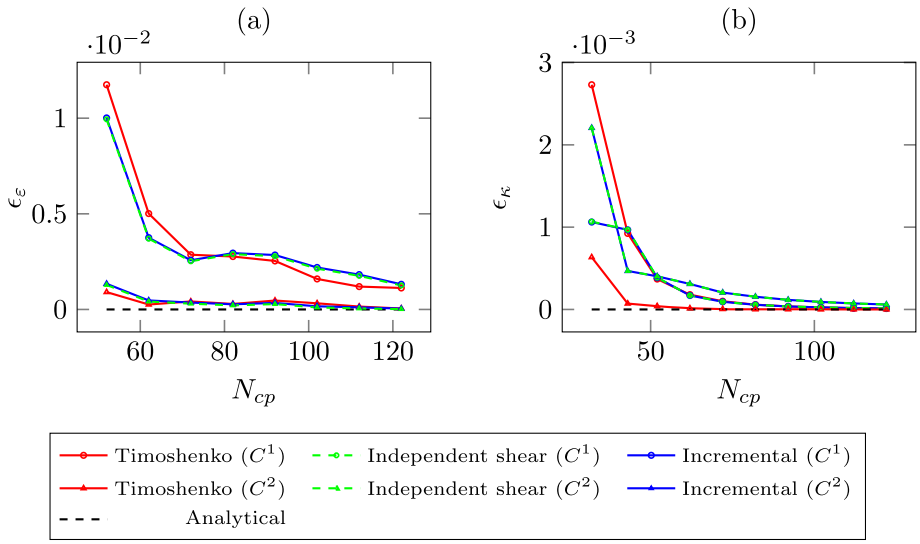

Fig. 13 Contact between the belt and a pulley—relative difference for different degrees of continuity: **(a)** axial strain at $s = L$; **(b)** curvature change at $s = L$

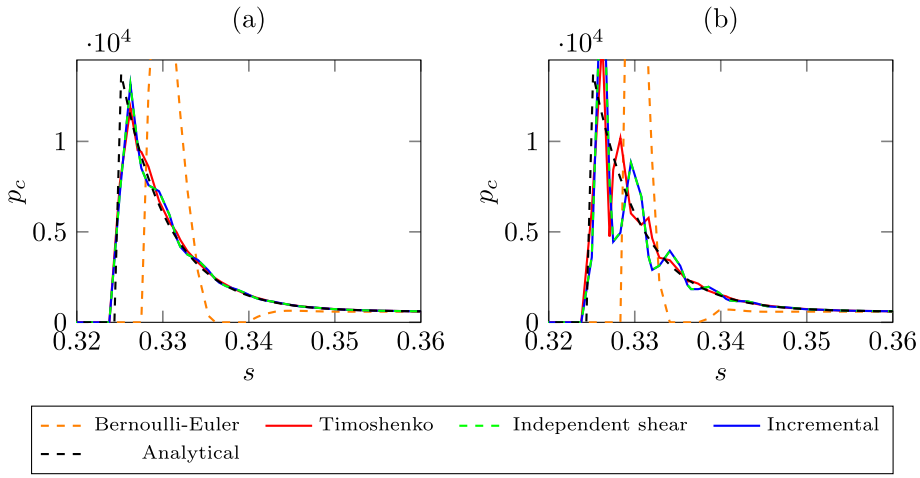

Fig. 14 Contact between the belt and the pulley—contact pressure distributions for different penalty parameters and uniform knot vector: **(a)** $\mathbb{C} = 10^{11}$; **(b)** $\mathbb{C} = 5 \cdot 10^{11}$

The results show that the obtained contact pressure distributions strongly depend on the choice of discretization and the penalty parameter. In general, improved convergence is achieved by increasing the interelement continuity and the polynomial order, which leads to a smoother representation of the contact response. When the contact domain is small, the local mesh refinement is especially advantageous, achieving accurate results with coarser meshes and reduced number of control points. This example also confirmed that the proposed approaches require less computational time than the classical Timoshenko model.

11 Conclusions

The key findings of this research are related to a novel approach for modelling shear-deformable rods at large deformations with a particular focus on contact problems. Making use of the computational efficiency of the unshearable Bernoulli-Euler model, we developed a novel kinematic description with the shear strain being the independent variable instead of the rotation angle as it is usual in the Timoshenko model. The respective computational scheme features a two stage procedure: first, the solution for the Bernoulli-Euler model is

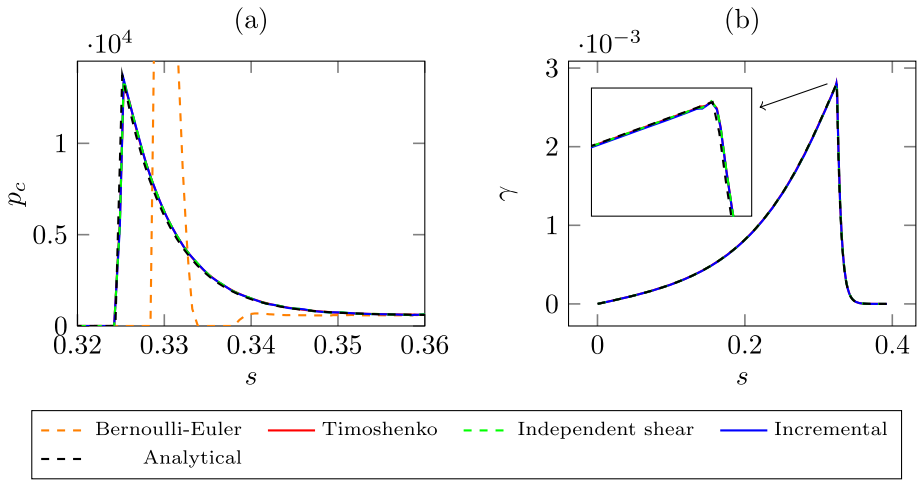

Fig. 15 Contact pressure between the belt and the pulley—non-uniform knot vector with refined mesh in the contact domain: **(a)** contact pressure distributions; **(b)** shear strain

obtained, and then further iterations with released unshearability constraint rapidly converge to a neighbouring solution. The total computational cost is demonstrated to be smaller than that of the Timoshenko model.

Furthermore, we make use of the smallness of the change in the deformed state because of "switching on" the shear compliance and develop another model by means of the incremental form of the equations of the rod theory. Having potential to provide accurate results with just a single linear correction step on top of the available Bernoulli-Euler solution, this scheme, however, still requires iterations within a Newton loop in case the problem set-up features essential nonlinearities like contact.

The numerical examples presented in the paper feature an isogeometric approximation of the kinematic variables with the benefit of freely choosing the continuity of the approximation. The efficiency and the accuracy of the newly developed models were demonstrated on several examples of increasing complexity, for which analytical solutions are available. Particular attention was paid to the convergence of the solutions with increasing number of variables in the discretized model as well as to the conditions, under which the important peaks in the contact pressure between the rod and the obstacle are accurately and efficiently reflected by the numerical models.

Acknowledgements The author acknowledges TU Wien Bibliothek, Austria for financial support through its Open Access Funding Programme.

Author contributions Conceptualization: J.K. and Y.V.; Implementation and numerical experiments: S.M.; Writing: S.M. and Y.V.; Editing: Y.V. and J.K.

Funding Open access funding provided by TU Wien (TUW). No funding was received for conducting this study.

Data availability No datasets were generated or analysed during the current study.

Open Access This article is licensed under a Creative Commons Attribution 4.0 International License, which permits use, sharing, adaptation, distribution and reproduction in any medium or format, as long as you give appropriate credit to the original author(s) and the source, provide a link to the Creative Commons licence, and indicate if changes were made. The images or other third party material in this article are included in the article's Creative Commons licence, unless indicated otherwise in a credit line to the material. If material is not included in the article's Creative Commons licence and your intended use is not permitted by statutory regulation or exceeds the permitted use, you will need to obtain permission directly from the copyright holder. To view a copy of this licence, visit http://creativecommons.org/licenses/by/4.0/.

Declarations

Conflict of interest The authors declare no conflict of interest.

References

1. Irschik, H., Gerstmayr, J.: A continuum mechanics based derivation of Reissner's large-displacement finite-strain beam theory: the case of plane deformations of originally straight Bernoulli-Euler beams. Acta Mech. **206**, 1–21 (2009). https://doi.org/10.1007/s00707-008-0085-8
2. Irschik, H., Gerstmayr, J.: A continuum-mechanics interpretation of Reissner's non-linear shear-deformable beam theory. Math. Comput. Moddel. Dyn. Syst. **17**(1), 19–29 (2011). https://doi.org/10.1080/13873954.2010.537512
3. Irschik, H.: Enhancement of elementary beam theories in order to obtain exact solutions for elastic rectangular beams. Mech. Res. Commun. **68**, 46–51 (2015). https://doi.org/10.1016/j.mechrescom.2014.08.005
4. Irschik, H.: Generalized reciprocity theorems for infinitesimal deformations superimposed upon finite deformations of rods: the plane problem. Acta Mech. **230**, 3909–3921 (2019). https://doi.org/10.1007/s00707-019-02429-4
5. Eliseyev, V.: The non-linear dynamics of elastic rods. J. Appl. Math. Mech. **52**(4), 493–498 (1988). https://doi.org/10.1016/0021-8928(88)90039-1
6. Vetyukov, Y.: Nonlinear Mechanics of Thin-Walled Structures: Asymptotic, Direct Approach and Numerical Analysis (Springer, 2014). https://doi.org/10.1007/978-3-7091-1777-4
7. Antman, S.: The Theory of Rods. In: Truesdell, C. (ed.) Linear Theories of Elasticity and Thermoelasticity, pp. 641–703. Springer, Cham (1973). https://doi.org/10.1007/978-3-662-39776-3_6
8. Antman, S.: Nonlinear Problems of Elasticity. In: Applied Mathematical Sciences, vol. 107. Springer, Cham (2005) https://doi.org/10.1007/0-387-27649-1
9. Wriggers, P., Zavarise, G.: On contact between three-dimensional beams undergoing large deflections. Commun. Numer. Methods Eng. **13**, 429–438 (1997). https://doi.org/10.1002/(SICI)1099-0887(199706)13:6<429::AID-CNM70>3.0.CO;2-X
10. Wriggers, P.: Computational Contact Mechanics, Second Edition. Springer (2006). https://doi.org/10.1007/978-3-540-32609-0
11. Meier, C., Wall, W., Popp, A.: A unified approach for beam-to-beam contact. Comput. Methods Appl. Mech. Eng. **315**, 972–1010 (2017). https://doi.org/10.1016/j.cma.2016.11.028
12. Franke, D., Düster, A., Nübel, V., Rank, E.: A comparison of the h-, p-, hp- and rp- version of the FEM for the solution of the 2D Hertzian contact problem. Comput. Mech. **45**, 513–522 (2010). https://doi.org/10.1007/s00466-009-0464-6
13. Essenburg, F.: On the significance of the inclusion of the effect of transverse normal strain in problems involving beams with surface constraints. J. Appl. Mech. **42**(1), 127–132 (1975). https://doi.org/10.1115/1.3423502
14. Naghdi, P., Rubin, M.: On the significance of normal cross-sectional extension in beam theory with application to contact problems. Int. J. Solids Struct. **25**(3), 249–265 (1989). https://doi.org/10.1016/0020-7683(89)90047-4
15. Vetyukov, Y., Oborin, E., Scheidl, J., Krommer, M., Schmidrathner, C.: Flexible belt hanging on two pulleys: contact problem at non-material kinematic description. Int. J. Solids Struct. **168**, 183–193 (2019). https://doi.org/10.1016/j.ijsolstr.2019.03.034
16. Scheidl, J., Vetyukov, Y.: Steady motion of a slack belt drive: dynamics of a beam in frictional contact with rotating pulleys. J. Appl. Mech. **87**(12), 121011 (2020). https://doi.org/10.1115/1.4048317
17. Scheidl, J., Vetyukov, Y.: Steady Motion of a Belt in Frictional Contact with a Rotating Pulley, pp. 209–217. Springer International Publishing, Cham, (2022). https://doi.org/10.1007/978-3-030-79325-8_18
18. Alciatore, D.G., Traver, A.E.: Multipulley belt drive mechanics: creep theory vs shear theory. J. Mech. Des. **117**(4), 506–511 (1995). https://doi.org/10.1115/1.2826711
19. Belyaev, A., Eliseev, V., Irschik, H., Oborin, E.: Nonlinear statics of extensible elastic belt on two pulleys. PAMM: Proc. Appl. Math. Mech. **16**, 11–14 (2016). https://doi.org/10.1002/pamm.201610004
20. Belyaev, A., Eliseev, V., Irschik, H., Oborin, E.: Contact of two equal rigid pulleys with a belt modelled as Cosserat nonlinear elastic rod. Acta Mech. **228**(12), 4425–4434 (2017). https://doi.org/10.1007/s00707-017-1942-0
21. Belyaev, A., Eliseev, V., Irschik, H., Oborin, E.: On static contact of belt with different pulleys. IOP Conf. Ser.: Mater. Sci. Eng. (2017). https://doi.org/10.1088/1757-899X/208/1/012004
22. Belyaev, A., Eliseev, V., Irschik, H., Oborin, E.: Static contact of belt and pulleys with account for shear and gravity. J. Phys: Conf. Ser. **1048**(1), 1–9 (2018). https://doi.org/10.1088/1742-6596/1048/1/012002
23. Echter, R., Oesterle, B., Bischoff, M.: A hierarchic family of isogeometric shell finite elements. Comput. Methods Appl. Mech. Eng. **254**, 170–180 (2013). https://doi.org/10.1016/j.cma.2012.10.018
24. Oesterle, B., Sachse, R., Ramm, E., Bischoff, M.: Hierarchic isogeometric large rotation shell elements including linearized transverse shear parametrization. Comput. Methods Appl. Mech. Eng. **321**, 383–405 (2017). https://doi.org/10.1016/j.cma.2017.03.031
25. Da Beirão, L., Veiga, T., Hughes, J., Kiendl, C., Lovadina, J., Niiranen, A., Reali, H.: Speleers: A locking-free model for Reissner–Mindlin plates: Analysis and isogeometric implementation via NURBS and triangular NURPS. Math. Models Methods Appl. Sci. (2017). https://doi.org/10.1142/S0218202515500402
26. Boyer, F., Lebastard, V., Candelier, F., Renda, F.: Dynamics of continuum and soft robots: a strain parameterization based approach. IEEE Trans. Rob. **37**(3), 847–863 (2020). https://doi.org/10.1109/TRO.2020.3036618
27. Hughes, T., Cottrell, J., Bazilevs, Y.: Isogeometric analysis: CAD, finite elements, NURBS, exact geometry and mesh refinement. Comput. Methods Appl. Mech. Eng. **194**(12), 4135–4195 (2005). https://doi.org/10.1016/j.cma.2004.10.008
28. Cotrell, J., Hughes, T., Bazilevs, Y.: Isogeometric Analysis: Toward Integration of CAD and FEA, 1st edn. Wiley, Hoboken (2009)
29. Cazzani, A., Malagù, M., Turco, E.: Isogeometric analysis of plane-curved beams. Math. Mech. Solids **21**, 562–577 (2016). https://doi.org/10.1177/1081286514531265
30. Borković, A., Kovačević, S., Radenković, G., Milovanović, S., Majstorović, D.: Rotation-free isogeometric dynamic analysis of an arbitrary curved plane Bernoulli–Euler beam. Eng. Struct. **181**, 192–215 (2019). https://doi.org/10.1016/j.engstruct.2018.12.003

31. Weeger, O., Wever, U., Simeon, B.: Isogeometric analysis of nonlinear Euler–Bernoulli beam vibrations. Nonlinear Dyn. **72**, 813–835 (2013). https://doi.org/10.1007/s11071-013-0755-5
32. Kiendl, J., Bletzinger, K.U., Linhard, J., Wüchner, R.: Isogeometric shell analysis with Kirchoff-Love elements. Comput. Methods Appl. Mech. Eng. **198**, 3902–3914 (2009). https://doi.org/10.1016/j.cma.2009.08.013
33. Radenković, G., Borković, A., Marussig, B.: Nonlinear static isogeometric analysis of arbitrarily curved Kirchhoff-Love shells. Int. J. Mech. Sci. **192**, 106143 (2021). https://doi.org/10.1016/j.ijmecsci.2020.106143
34. Lu, J.: Isogeometric contact analysis: geometric basis and formulation for frictionless contact. Comput. Methods Appl. Mech. Eng. **200**, 726–741 (2011). https://doi.org/10.1016/j.cma.2010.10.001
35. Temizer, I., Wriggers, P., Hughes, T.: Contact treatment in isogeometric analysis with NURBS. Comput. Methods Appl. Mech. Eng. **200**, 1100–1112 (2011). https://doi.org/10.1016/j.cma.2010.11.020
36. De Lorenzis, L., Temizer, I., Wriggers, P., Zavarise, G.: A large deformation frictional contact formulation using NURBS-based isogeometric analysis. Int. J. Numer. Meth. Engng **87**, 1278–1300 (2011). https://doi.org/10.1002/nme.3159
37. Dimitri, R., De Lorenzis, L., Scott, M., Wriggers, P., Taylor, R., Zavarise, G.: Isogeometric large deformation frictionless contact using T-splines. Comput. Methods Appl. Mech. Eng. **269**, 394–414 (2014). https://doi.org/10.1016/j.cma.2013.11.002
38. Weeger, O., Narayanan, B., De Lorenzis, L., Kiendl, J., Dunn, M.: An isogeometric collocation method for frictionless contact of Cosserat rods. Comput. Methods Appl. Mech. Eng. **321**, 361–382 (2017). https://doi.org/10.1016/j.cma.2017.04.014
39. Agrawal, V., Gautam, S.: Varying-order NURBS disretization: An accurate and efficient method for isogeometric analysis of large deformation contact problems. Comput. Methods Appl. Mech. Eng. **367**, 113125 (2020). https://doi.org/10.1016/j.cma.2020.113125
40. Elishakoff, I., Kaplunov, J., Kaplunov, E.: Stephen Timoshenko's letters to Paul Ehrenfest, recently discovered at the museum Boerhaave, Leiden, the Netherlands. Phil. Mag. (2025). https://doi.org/10.1080/14786435.2025.2570218
41. Piegl, L., Tiller, W.: The NURBS Book. Springer, Cham (1995). https://doi.org/10.1007/978-3-642-59223-2
42. Zou, Z., Hughes, T., Scott, M., Miao, D., Sauer, R.: Efficient and robust quadratures for isogeometric analysis: Reduced Gauss and Gauss–Greville rules. Comput. Methods Appl. Mech. Eng. **392**, 1–46 (2022). https://doi.org/10.1016/j.cma.2022.114722
43. Hughes, T., Reali, A., Sangalli, G.: Efficient quadrature for NURBS-based isogeometric analysis. Comput. Methods Appl. Mech. Eng. **100**(5–8), 301–313 (2010). https://doi.org/10.1016/j.cma.2008.12.004
44. Simo, J., Laursen, T.: An augmented Lagrangian treatment of contact problems involving friction. Comput. Struct. **42**(1), 97–116 (1992). https://doi.org/10.1016/0045-7949(92)90540-G
45. Gasmi, A., Joseph, P., Rhyne, T., Cron, S.: Closed-form solution of a shear deformable, extensional ring in contact between two rigid surfaces. Int. J. Solids Struct. **48**, 843–853 (2011). https://doi.org/10.1016/j.ijsolstr.2010.11.018

Publisher's Note Springer Nature remains neutral with regard to jurisdictional claims in published maps and institutional affiliations.